Submitted to the *Journal of Geophysical Research, Oceans*, February 14, 2001

Mesoscale Variability of SeaWiFS Satellite Ocean Color: Global Patterns and Spatial Scales

Scott C. Doney
National Center for Atmospheric Research, Boulder, Colorado

David M. Glover and Scott J. McCue
Woods Hole Oceanographic Institution, Woods Hole, Massachusetts

Montserrat Fuentes
North Carolina State University, Raleigh, North Carolina

Abstract
Using the semivariogram approach from geostatistics, we characterize for the first time the global patterns of mesoscale (approx. 10–200 km and days to a few weeks) ocean biological variability. The magnitude of the variability and length scale fields are reported for a full year of SeaWiFS ocean color data. The analysis shows a number of coherent geographical patterns across a wide range of biological and physical environments. When normalized to the mean chlorophyll as a coefficient of variation, the resolved mesoscale variance (relative sill) is approximately uniform in the tropics and subtropics (0.1–0.2), increasing to 0.3–1.0 in upwelling (Equatorial Pacific, coastal) and subpolar/polar regions, approximately scaling with the mean chlorophyll concentration. The unresolved variance (nugget), which includes submesoscale geophysical variability as well as instrument/algorithm noise, is inversely correlated with mean chlorophyll concentration in the oligotrophic subtropics (an indication of instrument/algorithm noise) reducing to a low background value (0.1) elsewhere. Mesoscale variance dominates ocean color variability in oligotrophic regimes and is a third to a half of the total variance even in regions with strong seasonality. The mesoscale spatial scale (range) is approximately zonal, with values of 200–350 km near the Equator to less than 50 km close to the poles similar to the physical scales estimated from altimeter sea surface height variability data and the first baroclinic Rossby deformation radius. Our results demonstrate the global generality of previous local and regional findings that physical mesoscale turbulence governs biological spatial scales both directly (e.g. stirring) and indirectly (e.g. nutrient injection). The same is not true, at least directly, for the (normalized) magnitude of the biological variability, which is not well correlated with mesoscale eddy kinetic energy and in particular does not show the characteristic west-east asymmetry associated with the western boundary currents. Regional deviations from these large-scale variance and spatial length-scales trends, for example lower range and higher resolved variance in coastal upwelling regimes, are explicable by the the characteristics of the biological-physical interaction in those environments.

1. Introduction

Routine measurements of ocean color from space provide for the first time a globally coherent, synoptic picture of the patterns and variability of upper ocean biology [*McClain et al.*, 1998]. The large-scale ocean color field, a proxy for surface layer phytoplankton chlorophyll concentrations, is governed by the seasonal distributions of light, nutrients, upwelling and upper ocean mixing [e.g. *Wroblewski et al.*, 1989; *McClain et al.*, 1990; *Mann and Lazier*, 1991; *Yoder et al.*, 1993]. On the mesoscale (approx. 10–200 km and a few days to weeks), ocean color variability is thought to be modulated by physical processes either directly by turbulent advection and stirring [e.g. *Steele*, 1978; *Mackas et al.*, 1985; *Abraham*, 1998] or indirectly via impacts on phytoplankton growth rates and trophic interactions [e.g. *Haury et al.*, 1978; *Mackas et al.*, 1985; *Garcon et al.*, 2001]. ¿From a global perspective, satellites provide the only feasible approach for mapping ocean surface chlorophyll at the required time and space scales to characterize mesoscale variability.

Using the semivariogram approach from geostatistics [*Journel and Huijbregts*, 1978], we calculate the mesoscale variance, subgridscale noise and measurement error, and spatial decorrelation length scales globally for a full year of SeaWiFS ocean color data [*McClain et al.*, 1998]. The spatial semivariogram, also called the structure function in probability [*Yaglom*, 1957] or meteorology [*Gandin*, 1963], provides a useful measure for quantifying biological–physical interactions [*Yoder et al.*, 1987; *Washburn et al.*, 1998; *Yoder et al.*, 2001] and discriminating among theoretical models. It is also a necessary component of future work to objectively analyze ocean color images using methods such as kriging [e.g. *Davis*, 1986; *Chelton and Schlax*, 1991]. A detailed description of the statistical techniques and preliminary results for a single month for the North Atlantic can be found in *Fuentes et al.* [2000]. Here we present the more extensive full annual and global analysis, focusing on relating the observed patterns to underlying physical and biological processes.

Theories about the physical and biological controls on ocean phytoplankton patchiness have a rich history (e.g. [*Denman and Platt*, 1976; *Steele*, 1978; *Okubo*, 1980; *Mackas et al.*, 1985; *Denman and Gargett*, 1995; *Robinson et al.*, 2001]). In the ocean submesoscale (0.5–10 km) and mesoscale (10–200 km), biological spatial structure is a dynamic balance between local and regional generation processes and downscale turbulent eddy transfer of variability from large to small scale, where it is eventually dissipated [*Mackas et al.*, 1985]. Physical and biological variability are often tightly coupled, though the biological expression does not always map onto the physical fields in a straightforward manner and can differ from variable to variable [*Yoder et al.*, 1993; *Abraham*, 1998; *Archer and Mahavaden*, 2000]. Physical turbulence by itself can only create patterns from existing gradients set-up from differential net growth, removal or accumulation. Ocean physics, however, is often also a key driver of phytoplankton growth rates through nutrient enrichment, vertical velocities and modulation of the mixed layer depth and thus mean light field.

A now classic example is the formation of phytoplankton blooms near the edges of meandering surface baroclinic jets [*Woods*, 1988]. The increased phytoplankton growth rates are triggered by high nutrient input and reduced mixed layer depth due to intense submesoscale upwelling (and downwelling) velocities along the flanks of the jet, and the resulting phytoplankton blooms are elongated into complex, filament like structures [*Spall and Richards*, 2000; *Lima et al.*, 2001]. At somewhat larger spatial scale, doming of isopycnals by cyclonic and mode water eddies brings subsurface nutrients into the euphotic zone leading to elevated chlorophyll levels and enhanced new and primary production in oligotrophic regimes [*McGillicuddy and Robinson, 1997*; *McGillicuddy et al.*, 1998; *Archer and Mahavaden*, 2000]. Submesoscale eddy-eddy interaction is likely also involved in this so-called "eddy-pumping" mechanism.

A similar phenomenon, but with iron not macronutrients, has been observed with tropical instability waves in the Equatorial Pacific [*Yoder et al.*, 1994]. Vertical nutrient inputs and enhanced biomass accumulation have also been proposed recently on larger spatial scales associated with westward propagating, planetary Rossby waves [*Cipollini et al., 2001*; *Uz et al.*, 2001] *Levy et al.* [1998] suggest that a combination of nutrient and light (mixed layer depth) limitation are responsible for transient phytoplankton blooms following the collapse and baroclinic adjustment of deep convective chimneys in the northwest Meditteranean, and *Smith et al.* examine the role of wintertime mixed layer depth variability on the subsequent development of an open-ocean spring bloom, though they found the magnitude of the effect to be rather small.

Because of their high spatial (and sometimes temporal) resolution, satellite ocean color images from the CZCS [*Feldman et al.*, 1989] and more recently the SeaWiFS [*McClain et al.*, 1998] instruments are invaluable for characterizing the mesoscale time/space variability of ocean biology [e.g. *Abbott and Zion, 1985*; *Barale et al.*, 1986; *Muller-Karger and Castro*, 1994] (see also [*Yoder*, 2000] for a recent review). Based on spectral analysis of LANDSAT surface reflectance images for example, *Gower et al.* [1980] suggest that mesoscale phytoplankton patchiness is governed by physical advection. *Denman and Abbott* [1988] and *Denman and Abbott* [1994] use auto-spectra and cross-spectra analysis of CZCS and AVHRR sea surface temperature data off coastal California to demonstrate strong similarity in the characteristic biological and physical time-scales. Qualitative and quantitative analysis of satellite ocean color and 1-D surface transects shows a similar correspondence for spatial variability [*Yoder et al., 1987*; *Smith et al.*, 1988; *Yoder et al.*, 1993; *Washburn et al.*, 1998; *McGillicuddy et al.*, 2001; *Yoder et al.*, 2001]. These and other studies, however, have been conducted for small regions of the ocean and, for CZCS data in particular, restricted mostly to coastal environments.

Spectral analysis and geostatistical techniques are two of the more common methods for computing spatial scales from oceanographic scales. While quite powerful, spectral methods have a number of drawbacks including problems with missing data (most of the spectral analyses discussed above were conducted on carefully chosen, cloud free images) and potential ambiguities over the interpretation of spectral slopes (e.g. [*Fasham*, 1976]). Geostatistical techniques (or as discussed below closely related correlation analysis) provide less detailed information but should be more robust for typical geophysical data [*Chelton and Schlax*, 1991; *Fuentes et al*, 2000].

The SeaWiFS ocean color satellite data set used in this study and the necessary geostatistical tools, including the robust empirical semivariogram and semivariogram models, are described in Section 2. In Section 3, we discuss in detail an example calculation of the semivariogram approach for a single $5° \times 5°$ area. We then present the global patterns of ocean color mesoscale variability and spatial scales over an annual cycle followed by a summary and discussion (Section 4).

2. Data and Methods

2.1. SeaWiFS Ocean Color

The Sea-viewing Wide Field of view Sensor (SeaWiFS) ocean color instrument [*Hooker and Esaias*, 1993; *McClain et al.*, 1998] provides near-global coverage every 2 days of upwelled radiance for eight spectral bands in the visible and near-infrared. Surface ocean chlorophyll concentrations (Chl mg m^{-3}) are calculated from the ratios of different water-leaving visible bands using ground-truthed empirical algorithms [*O'Reilly et al.*, 1998]. In addition to the required atmospheric corrections, pixels with land, clouds or heavy aerosol loading are removed prior to the calculation of surface chlorophyll. Continuous Global Area Coverage (GAC) data with a nominal resolution of 4 km $\times$ 4 km is subsampled from the raw 1 km $\times$ 1 km data and is stored aboard the spacecraft for later transmission to ground stations.

Here we use Level 3 daily standard mapped images (version 2), which are projections of the GAC data onto a global, equal-angle grid ($2\pi/2048$) with a nominal 9 km $\times$ 9 km resolution. The natural log transformation ln(Chl) is applied to the data following the arguments of *Campbell* (1995) that oceanic bio-optical variability is distributed approximately log-normally. To avoid spurious effects in the semivariogram [*Clark*, 1979; *Cressie*, 1993], large-scale spatial trends are removed by subtracting monthly mean fields smoothed with a moving two-dimensional 24×24 pixel spatial filter (equivalent to about 200x200 km scale at the equator or roughly $2° \times 2°$). The resulting detrended data are refered to as the daily anomalies. We have investigated the impact of using a monthly block time averages rather than running time averages (still with a one month window). The differences are minimal except for very high latitudes (poleward of 60 deg.) in the spring/summer season, where the monthly block average leads to somewhat higher total variances.

2.2. Semivariogram Analysis

The semivariogram or structure function $\gamma(\mathbf{v})$ measures the local spatial variation of geophysical data $Z(x)$, describing how samples are related with vector distance $\mathbf{v}$ (*Journel and Huijbregts*, 1978):

$$\gamma(\mathbf{v}) = \frac{1}{2}\mathrm{var}\{Z(\mathbf{x}+\mathbf{v}) - Z(\mathbf{x})\}. \quad (1)$$

The semivariogram is closely related to the covariance function. In general, two neighboring points are more likely to have similar values than sample pairs farther apart. Thus the semivariogram (covariance) function will have low (high) values at small spatial lags, increasing (decreasing) with distance. Beyond some distance, the data points can often be assumed to be uncorrelated or independent, in which case the semivariogram approaches a uniform variance while the covariance function goes to zero.

Because of clouds and other problems leading to incomplete spatial sampling, the ocean color semivariogram must be computed empirically [*Matheron* 1971]. We use a robust (to contamination by outliers) semivariogram estimator proposed by *Cressie and Hawkins* [1980]:

$$\bar{\gamma}(\mathbf{v}) = \frac{\frac{1}{2}\left(\frac{1}{N(\mathbf{v})}\sum_{N(\mathbf{v})}|Z(\mathbf{x}_i) - Z(\mathbf{x}_j)|^{1/2}\right)^4}{\left(0.457 + \frac{0.494}{N(\mathbf{v})}\right)}, \qquad (2)$$

where $N(\mathbf{v})$ is the number of data points seperated by vector distance $\mathbf{v}$. In the robust estimator, the spatial difference is transformed into an approximate Gaussian form prior to computing the semivariances (see also [*Cressie*, 1993] and [*Fuentes et al.*, 2000]).

Semivariograms are computed numerically for each month of 1998 for $5° \times 5°$ areas over the globe, the size chosen after some experimentation to minimize the spatial heterogeneity of the ocean color data while retaining sufficient spatial extent to resolve the full span of the mesoscale (10 km–200 km). For each day, the surface chlorophyll pixels (daily anomalies) within the box are sorted to find all possible combinations of valid data pairs in the zonal (E-W) and meridional (N-S) directions. Separate semivariograms versus distance (in km) are then calculated using Equation 2 in the two directions to highlight anisotropy. A discretized version of equation 2 is used, with the approximate spatial bin size (nominally 9 km) differing with direction and latitude. The daily semivariance estimates at each distance lag are then aggregated over the month weighted by the number of valid data pairs.

Semivariograms are rarely used in their original form but rather are fit with simple statistical models to extract the desired information [*Journel and Huijbregts*, 1978], and we have chosen to use the spherical model: $\hat{\gamma}(\mathbf{v}) =$

$$\begin{cases} 0 & \mathbf{v} = 0, \\ c_0 + (\sigma^2 - c_0)\left\{\frac{3}{2}\frac{\mathbf{v}}{r} - \frac{1}{2}\left(\frac{\mathbf{v}}{r}\right)^3\right\} & 0 < \mathbf{v} \le r, \\ \sigma^2 & \mathbf{v} > r, \end{cases} \qquad (3)$$

because of its common use and simple interpretation [*Clark*, 1976]. An example is shown in Figure 1. The idealized spherical model has a (typically) small value near the origin set by the nugget c_0, the unresolved, subscale variance and/or measurement error at zero lag. The semivariance then increases with distance out to the range r, at which point samples are essentially uncorrelated and the model curve plateaus at the value of the total sill σ^2. A fourth parameter, the relative sill σ^2_{rel}, can be defined as that part of the total variance resolved by the observations

$$\sigma^2_{\mathrm{rel}} = \sigma^2 - c_0 \qquad (4)$$

and which is attributable to geophysical processes.

For each $5° \times 5°$ area, the spherical model is fit to the monthly semivariograms using a modified version of the Levenberg-Marquardt nonlinear least-squares regression [*Press et al.*, 1992], and the model parameters (nugget, range, total and relative sill), estimated errors, and correlation coefficients are stored as final output. Before and during the nonlinear fit the semivariances are passed through a series of tests to remove the results from those $5° \times 5°$ cells that appear either non-geostatistical and/or overly contaminated by noise. A minimum of 30 valid data pairs are required at each spatial lag, and atleast 4 spatial lags must be represented in order to fit the model. The spherical model parameters are retained only if the Levenberg-Marquardt method converges, the correlation coefficent has a statistical significance level greater than 95%, and the fit parameters do not imply any non-geostatistical results (total sill less than nugget, negative range, negative nugget). As a final test, the relative standard deviations of each model parameter must be less than 200% and the range not exceed the size of the 5° cell. In certain cases the above fit is performed while forcing the nugget to be zero; this is done when all other tests were positive except the negative nugget restriction.

The empirical semivariogram and model values in Figure 1 and throughout the remainder of the paper are translated into coefficients of variation in geophysical space (mg Chl m^{-3}), i.e. the geophysical standard deviations divided by the means. The coefficient of variation has several desirable qualities for a log-normally distributed variable. In particular if the variability scales with the geophysical mean, as might be expected at least roughly on theoretical grounds, then the coefficient of variance will be uniform even over large variations in mean concentrations such as observed for surface ocean chlorophyll.

3. Results

3.1. Example calculation

To better illustrate the semivariogram structure function approach, we first discuss in detail the results for an example $5^\circ \times 5^\circ$ area before moving on to the global patterns. Figure 2a displays the smoothed, monthly geometric mean SeaWiFS chlorophyll composite for June, 1998 over a region of the South Pacific with relatively low mean chlorophyll concentrations. The coverage from a single day for the region is shown in Figure 2b. The $5^\circ \times 5^\circ$ area bounded by 105–110°W by 30–35°S used in the analysis is outlined in the figure. The monthly composite data show large-scale trends associated with the edge of the subtropical gyre. As demonstrated by the individual daily image, cloud contamination and orbital sampling constraints would complicate traditional spatial structural analysis techniques such as spectral analysis. Mesoscale features are evident in the daily image but with some background noise, much of it associated with cloud–ocean transitions. The distribution of the daily chlorophyll values over the month are approximately Gaussian once the log-transform is applied (not shown), consistent with previous findings [*Campbell*, 1995] and supporting our normalization procedure.

The monthly east–west semivariogram for the $5^\circ \times 5^\circ$ area is shown in Figure 1. Although there is considerable scatter in the individual daily semivariance estimates at any particular distance (not shown) [*Fuentes et al.*, 2000], the monthly semivariogram follows a well-defined curve that is closely approximated by the spherical model (r^2 =0.957). The estimated values for the model parameters are range (150 km), nugget (0.22), total sill (0.31), and relative sill (0.09). The nonlinear regression routine provides estimates of the errors in these parameters, but since the semivariances themselves are not statistically independent these errors estimates are undoubtably overestimates and not reported here. The high nugget relative to the sill suggest that the unresolved variance at this location is large, and as discussed below is likely associated with instrument and algorithmic uncertainties. The behavior of the semivariogram at short spatial lags (roughly <20 km in Figure 1) is not as well characterized as one perhaps would wish from the global Level 3 data (nominal resolution of 9km), and the estimated nugget is sensitive to the fit through one or two data points near the origin.

The mesoscale variability for the $5^\circ \times 5^\circ$ area shows a directional anisotropy, with the estimated range in the north– south direction being ~230 km. The gradient in the large-scale chlorophyll field for this region is also oriented approximately north–south, and the larger range calculated in that direction may reflect a partial aliasing of the nonstationarity in the mean, despite the removal of the smoothed monthly field. The total sill parameter (partial sill plus nugget) is approximately the same in each direction (E-W 0.31 *vs.* N-S: 0.35) as is the nugget (0.22 in both directions).

3.2. Variance, relative sill and nugget

Turning to the global distributions, one of the goals of our research is to see whether we can relate the spatial structure function of ocean chlorophyll mesoscale variability to patterns of physical and biological variables. The global annual mean SeaWiFS ocean color distribution for 1998 (Figure 3a) shows quite clearly the strong relationship between the large-scale patterns of ocean biomass and the vertical macro-nutrient supply modulated by aeolian deposition and subsurface sources of micro-nutrients such as iron [*Mann and Lazier*, 1991; *Fung et al.*, 2000; *Archer and Johnson*, 2000; *Moore et al.*, 2001]: low levels in the convergent subtropical gyres; higher concentrations in the coastal upwelling regions and subpolar latitudes of the North Atlantic and western North Pacific; and intermediate levels in the iron-limited high nitrate-low chlorophyll regions of the Equatorial Pacific and Southern Ocean. Note also the large variations in open-ocean surface chlorophyll concentration spanned by the standard logarithmic color bar, covering almost two orders of magnitude in the open ocean.

The second panel in Figure 3 shows the total standard deviation (also as coefficent of variation) of the daily level 3 SeaWiFS ocean color data. The total standard deviation varies over a wide range, from a minimum of 0.3–0.5 (30–50%) in some oligotrophic areas to greater than 1.0 (100%) in coastal upwelling and high latitude bloom regions. Elevated relative variability (> 0.6) is also observed along frontal boundaries (e.g. Equatorial Pacific, subpolar/subtropical transitions) and in regions large ocean color seasonality (e.g. Arabian Sea, subpolar North Atlantic) [*Yoder et al.*, 1993].

The coefficent of variation of daily anomalies (Figure 3c), by contrast, is generally more uniform over the open ocean, with values of about 0.3–0.5 (30–50%) except for coastal, localized high latitude, and (as discussed below) some very oligotrophic (e.g. eastern South Pacific) regions. Since the large-scale seasonal cycle is removed in the creation of the daily anomalies, Figure 3c quantifies only the contribution of variability occuring on time-scales of less than one month and spatial scales of less than 2°, which we attribute to mesoscale processes (plus unresolved noise and submesoscale effects). Translated into absolute, geophysical units (mg Chl m^{-3}), the result demonstrates that mesoscale ocean color variability is approximately (but not linearly as shown below) proportional to the total amount chlorophyll present. This result, while perhaps not overly surprising for a lognormally distributed variable, places quantitative constraints on the magnitude of the inherent and forced mesoscale biological variability in the ocean.

The total variance (power) is displayed in Figure 4 divided into the fractions associated with the seasonal cycle and submonthly (meoscale) variability, respectively. The mesoscale signal dominates in the oligotrophic gyres but is a much smaller fraction (30–40%) of the overall variance in the subpolar gyres, Arabian Sea, Equatorial Pacific and subtropical/subpolar transition regions noted above.

In regions of strong seasonality, the computation of the daily anomalies using smoothed, block monthly composities could potentially introduce problems with the temporal scale seperation in Figures 3 and 4. To explore this effect, we have recomputed the daily anomalies using smoothed, sliding (one month window) time averages. The coefficents of variation for the daily anomalies are almost identical except for high latitudes in the summer season, where the block average is biased somewhat higher (not shown). This would be expected if the mean chlorophyll concentration changed rapidly over the month resulting in too large or small daily anomalies at the beginning and end of the month. However, the general spatial patterns for the two techniques are nearly identical, with elevated high latitude variability in the sliding mean case as well. Further, the semivariance estimator (Equation 2) is applied only to differences within daily images and is thus insensitive to mean offsets in the daily anomaly fields (which would, however, get aliased into the block time mean variance estimate), as would occur as the chlorophyll over the whole $5^{\circ} \times 5^{\circ}$ block rose and fell with the seasonal cycle.

The results of the semivariogram analysis for the 1998 SeaWiFS data are presented in Figure 5. The semivariogram further partitions the mesoscale variability in the daily anomalies Figure 3c into resolved (relative sill) and unresolved/noise (nugget) components. The relative sill values (Figure 5b) in the subtropics and tropics are approximately uniform and relatively low (about 0.1–0.2). Moderately larger values are observed in a band across the Equatorial Pacific and in the subpolar gyres while high values are observed along the coasts (particularly in coastal upwelling regimes) and at high latitudes. Strikingly, one sees only a weak signature in the ocean color results (Figure 3c and Figure 5b) of the strong east-west asymmetries associated with the high eddy kinetic energy regions of the mid-latitude western boundary current systems such as the Gulf Stream of Kuroshio [e.g. *Stammer*, 1997; 1998].

A scatter plot of the coefficient of variation of the relative sill versus the mean chlorophyll concentration (Figure 6a) shows essentially similar findings: low and uniform relative sills for annual mean chlorophyll concentrations less than 0.1 mg Chl m^{-3} growing in an approximate linear fashion with ln(Chl) above that value. High latitude cells (poleward of 60 deg.) are seperated out in (Figure 6a) because of potential sampling and SeaWiFS data processesing issues (e.g. low sun angle, sea-ice, cloud cover, seasonal bias, Level 3 bin aspect ratio). Although the polar relative sill values are generally high, likely due to summer season bias and more coastal values, they show generally the same relationship to mean chlorophyll data and our current conclusion is that the large relative sills at high latitude are likely real.

The spatial pattern of the annual mean nugget or unresolved variance (Figure 5c) is opposite in sense to that of the relative sill, high in the subtropics and low at mid- to high latitude, but with a much smaller overall magnitude. As shown by a scatter plot against annual mean chlorophyll (Figure 6b), the nugget is inversely correlated with ln(Chl) at low chlorophyll levels, and in fact, for mean chlorophyll values less than 0.1 mg m^{-3} the nugget generally exceeds the relative sill. Note that the nugget estimate refers only to point variability in the satellite signal (water leaving radiance, atmospheric transmission, instrument noise etc.) and is lower than the actual error in estimating surface water chlorophyll (~35% between 0.3–3.0 mg m^{-3} with larger error outside that range [*Hooker and McClain*, 2000]), which accounts for fluctuations and biases in the radiance–chlorophyll relationship as well [e.g. *O'Reilly et al.*, 1998].

A simple model for the spatially unresolved variance in the SeaWiFS data could be expressed as:

$$c_0 = \epsilon^2_{\text{observation}} + \epsilon^2_{\text{submesoscale}} \quad (5)$$

assuming that instrument/algorithm noise ($\epsilon^2_{\text{observation}}$) and submesoscale geophysical noise ($\epsilon^2_{\text{submesoscale}}$) sources are independent. The effective cut off between the resolved and unresolved geophysical signal, the latter of which we are calling submesoscale, from the semivariogram technique is grid dependent and at least one spatial lag if not more (or nominally 9km). Thus by this technique, a significant fraction of the submesoscale variability will be partitioned into the nugget. One interpretation of the nugget versus mean chlorophyll scatter diagram (Figure 6b), then, is that there is a error source proportional to the mean (approximate 0.1 coefficient of variation), which could arise as a combination of observational and submesoscale processes, together with a roughly constant, background variability in geophysical space. The latter process would become more dominant at very low chlorophyll values leading to the observed inverse correlation. Based on the spatial resolution of the Level 3 data alone, we can not distinguish whether this is background instrument derived or submesoscale, for example an episodic submesoscale feature of a particular magnitude irrespective of mean chlorophyll concentrations. We argue, however, from visual inspection of individual images that the instrument/algorithm source is more likely, for example due to satellite memory effects at opean ocean/cloud transitions (e.g. Figure 2b).

3.3. Spatial length-scale

The zonal spatial range field (Figure 5a) exhibits a strong, banded latitudinal pattern with maximal values of 250–300 km along the Equator decreasing poleward to less than 50 km near the poles. The latitudinal decrease in biological spatial scales is similar to results for physical mesoscale variability, suggesting that a common mechanism (eddy-generation by baroclinic instability) may be responsible. For example, *Smith et al.* [2000] using high-resolution, eddy-resolving numerical simulations of the North Atlantic, found that the zonal-average physical eddy autocorrelation spatial scales decreased from approximately 250 km at the Equator to about 40 km at 60°N. Similar spatial autocorrelation lengths have been calculated from satellite observations using TOPEX/Poseidon altimeter sea-surface height data globally (*Fu and Smith*, 1996; *Stammer*, 1997] and from Advanced Very High Resolution Radiometer (AVHRR) sea-surface temperature imagery for the eastern North Atlantic from 35°N to 60°N [*Krauss et al.*, 1990].

The physical eddy spatial scales outside the tropics vary roughly proportional (though not identical) to the Rossby deformation radius [*Krauss et al.*, 1990; *Stammer*, 1997; *Smith et al.*, 2000], the horizontal scale where rotation becomes important relative to buoyancy and a key parameter governing turbulent ocean flow [*Emery et al.*, 1984; *Chelton et al.*, 1998]. This finding has been argued as support for the hypothesis that the baroclinic instability of the density field is the primary processes driving mesoscale eddy formation. A similar correspondence for ocean color spatial scales is demonstrated in Figure 7, a plot of the zonal averages of the east–west and north–south range as well as Rossby radius (from [*Chelton et al.*, 1998]).

The east–west and north–south ocean color ranges are comporable in the tropics (Figure 7), but the east–west values tend to decrease more rapidly toward the poles. Note that the north-south ranges becomes more more difficult to compute at higher latitudes from the SeaWiFS L3m gridded data because the geophysical spatial scales are decreasing while the grid resolution in the north-south direction remains constant. In the east-west dimension (used in the zonal range calculation) the data grid size decreases with cosine latitude. The original binned data product, while using equal area grid cells, offers other computational difficulties. Further problems may arise because away from the coasts the main spatial gradients in chlorophyll are approximately north-south, and errors in removal of the large-scale spatial trends can be aliased into the semivariogram range estimate [*Fuentes et al.*, 2000].

In the North Atlantic, somewhat larger zonal spatial ranges are found in the west than in the east (Figure 5a), the opposite to the trend reported by *Fuentes et al.* [2000] from a single latitude band and single month. The asymmetry could reflect longer spatial scales of Gulf Stream meanders and rings but is not as clearly defined for the other western boundary currents. The coastal upwelling regions (e.g. Beguala current, California Current, Peru), which show large mesoscale variability, are notable exceptions to the overall latitudinal range patterns, with markedly lower ranges in both the east–west and north–south directions. The time/space space scales in these upwelling regions are smaller, often associated with sharp off-shore gradients and episodic upwelling jets and filaments [*Abbott and Zion*, 1987].

4. Summary and Discussion

Our analysis of the mesoscale variability of global SeaWiFS ocean color data shows a number of coherent geographical patterns across a wide range of biological and physical environments. When normalized to the mean chlorophyll as a coefficient of variation, the resolved mesoscale variance (relative sill) is approximately uniform in the tropics and subtropics (0.1–0.2), increasing to 0.3–1.0 in upwelling (Equatorial Pacific, coastal) and subpolar/polar regions, approximately scaling with the mean chlorophyll concentration. The unresolved variance (nugget), which includes submesoscale geophysical variability as well as instrument/algorithm noise, is inversely correlated with mean chlorophyll concentration in the oligotrophic subtropics (an indication of instrument/algorithm noise) reducing to a low background value (0.1) elsewhere. Mesoscale variance dominates ocean color variability in oligotrophic regimes and is a third to a half of the total variance even in regions with strong seasonality. The mesoscale spatial scale (range) is approximately zonal, with values of 200–350 km near the Equator to less than 50 km close to the poles similar to the physical scales estimated from altimeter sea surface height variability data and the first baroclinic Rossby deformation radius.

Our results demonstrate the global generality of previous local and regional findings that physical mesoscale turbulence governs biological spatial scales. The same is not true, at least directly, for the (normalized) magnitude of the biological variability, which is not well correlated with mesoscale eddy kinetic energy and in particular does not show the strong characteristic west-east asymmetry associated with the western boundary currents. Regional deviations from these large-scale variance and spatial length-scales trends, for example lower range and higher resolved variance in coastal upwelling regimes, are explicable by the the characteristics of the biological-physical interaction in those environments.

Quantifying the ocean color mesoscale structure function has a number of practical applications. First, quantifying the structure function is fundamental for any time/space objective analysis of the ocean color data set, a serious issue given the amount of missing data due to cloud cover etc. As demonstrated by *Chelton and Schlax* [1991], optimal (unbiased) time averages of a series of satellite images could only be accomplished by using *a priori* knowledge of the variance and correlation (structure) functions of the satellite signal. Second and related, the information inherent in a structure function is required in order to create the cost function (weighting of model data misfit) for data assimilation *U.S. Joint Global Ocean Flux Study, JGOFS*, 1992]. Third, the variance and spatial range estimates provide key constraints for the emerging field of basin (and soon global) eddy resolving ecosystem simulations [*Oschlies and Garcon*, 1998; *McGillicuddy et al.*, in prep.]. Much as satellite altimeter sea surface height variability has done for physical models [*Smith et al.*, 2000], maps of mesoscale ocean color statistics will highlight the deficiencies of current generation models and spur improvements (either in biological parameterizations and/or spatial resolution). Validated physical fields and eddy statistics likely may be a necessary but not sufficient condition for accurate biological dynamics (e.g. if significant nutrient input is occurring at the submesoscale).

Further work is needed in a number of areas to clarify some of the questions raised here. The behavior of the ocean color semivariogram at short spatial lags ($<$ 15 km) is not well characterized using the GAC Level-3 standard mapped images product, and thus we cannot clearly separate the effects of submesoscale variability from instrumental and algorithm noise. For that, we will have to turn to the higher resolution Local Area Coverage (LAC) data at the full SeaWiFS nominal resolution of 1 km $\times$ 1 km or alternatively the high resolution MODIS data. Semivariograms based on the LAC data will be particularly useful in light of recent very high resolution (1 km $\times$ 1 km) numerical results from an idealized, mesoscale jet experiment [*Levy et al. 2000*] showing that the magnitude of the transient phytoplankton blooms continue to grow as model resolution is decreased into the submesoscale (with no closure as of the writing of this paper).

The smaller sampling size of the LAC data should retain more of the original variance of the data leading to semivariograms with higher sills in addition to altered shapes at short lags. Further, the LAC data will allow us to experiment with reducing the size of the semivariogram averaging box providing better resolution near continental boundaries and other specific features. Relating the semivariogram results between the two resolutions, the so-called change of support or regularization problem [*Clark*, 1979], is not completely straightforward for the SeaWiFS data because of various data processing issues [*Campbell et al.*, 1995; *Fuentes et al.*, 2000]. We have begun a preliminary submesoscale analysis to be reported in a later publication.

Finally, our treatment here neglects any discussion of the temporal correlation scales. The Eulerian temporal decorrelation time-scale has as much to do with the rates of physical circulation as biological processes [*Denman and Abbott*, 1994]. But combined with Lagrangian decorrelation time-scales computed from drifters (e.g. [*Abbott et al.*, 1995; *Abbott and Letelier*, 1998]), the satellite time-scale data will certainly be useful. In addition, a number of researchers (e.g., [*Chelton and Schlax,* 1991]) propose local, temporal (rather than spatial) objective analysis as a simpler, more straightforward method of the interpolation of patchy satellite geophysical data such as ocean color.

Acknowledgments. A number of colleagues have contributed to this paper through comments and discussions over the last several years. In particular we would like to thank T. Hoar, I. Lima, D. McGillicuddy, J.K. Moore, D. Nychka, and D. Siegel. M. Fuentes acknowledges the support of the NCAR Geophysical Statistics Project, and S. Doney and D. Glover are supported in part by NASA SeaWiFS Grants W-19,223 and NAG-5-6456. This work would not be possible without the dedicated efforts of the NASA SeaWiFS project team (http://seawifs.gsfc.nasa.gov/SEAWIFS.html). Ocean color data used in this study were produced by the SeaWiFS Project at Goddard Space Flight Center. The data were obtained from the Goddard Distributed Active Archive Center. Use of this data is in accord with the SeaWiFS Research Data Use Terms and Conditions Agreement. The National Center for Atmospheric Research is sponsored by the National Science Foundation. This is WHOI contribution no. XXXXX.

References

Abbott, M.R., K.H. Brink, and L.A. Codispoti, Scales of variability of bio-optical properties as observed from near-surface drifters, *J. Geophys. Res.*, **100**, 13345–?, 1995.

Abbott, M.R. and Letelier, R.M., Decorrelation scales of chlorophyll as observed from bio-optical drifters in the California current, *Deep-Sea Res., II*, **45**, 1639–1667, 1998.

Abbott, M.R. and P.M. Zion, Satellite observations of phytoplankton variability during an upwelling event, *Cont. Shelf Res.*, **4**, 661–680, 1985.

Abbott, M.R. and P.M. Zion, Spatial and temporal variability of phytoplankton pigment off northern California during coastal ocean dynamics experiment, *J. Geophys. Res.*, **92**, 1745–1755, 1987.

Barlae, V., C.R. McClain, and P. Malanotte-Rizzoli, Space and time variability of the surface color field in the Northern Adriatic Sea, *J. Geophys. Res.*, **91**, 12957–12974, 1986.

Campbell, J.W., The lognormal distribution as a model for bio-optical variability in the sea., *J. Geophys. Res.*, **100**, 13,237–13,254, 1995.

Campbell, J.W., J.M. Blaisdell, and M.Darzi, Level-3 SeaWiFS data products: Spatial and temporal binning algorithms. SeaWiFS Tech. Rep. 32, NASA Tech. Mem. 104566, Goddard Space Flight Center, Greenbelt, Maryland, 77pp plus 3 plates, 1995.

Chelton, D. B. and M. G. Schlax, Estimation of time averages from irregularly spaced observations: with application to coastal zone color scanner estimates of chlorophyll concentration. *J. Geophys. Res.*, **96**, 14,669–14,692, 1991.

Chelton, D.B., R.A. deSzoeke, M.G. Schlax, K.E. Naggar, and N. Siwertz, Geographical variability of the first baroclinic Rossby radius of deformation, *J. Phys. Oceanogr.*, **28**, 433–460, 1998.

Cipollini, P., D. Cromwell, P.G. Challenor and S. Raffaglio, Rossby waves detected in global ocean colour data, *Geophys. Res. Lett.*, **28**, 323–326, 2001.

Clark, I., *Practical Geostatistics*, Elsevier Applied Science, New York, 1979.

Coale, K.H. *et al.*, A massive phytoplankton bloom induced by an ecosystem-scale iron fertilization experiment in the equatorial Pacific. *Nature*, *383*, 495–501, 1996.

Cressie, N.A.C. and Hawkins, D.M., Robust estimation of the variogram, I, *J. Int. Assoc. Math. Geology*, **12**, 115–125, 1980.

Cressie, N.A.C., When are relative variograms useful in geostatistics?, *J. Int. Assoc. Math. Geology*, **17**, 693–701, 1985.

Cressie, N.A.C., *Statistics for Spatial Data*, Wiley, New York, 1993.

Davis, J.C., *Statistics and Data Analysis in Geology*, Wiley, New York, 1986.

Denman, K.L. and M.R. Abbott, Time evolution of surface chlorophyll patterns from cross-spectrum analysis of satellite color, *J. Geophys. Res.*, **93**, 6789–6998, 1988.

Denman, K.L. and M.R. Abbott, Time scales of pattern evolution from cross-spectrum analysis of advanced very high resolution radiometer and coastal zone color scanner imagery, *J. Geophys. Res.*, **99**, 7433–7442, 1994.

Denman, K.L. and A.E. Gargett, Biological-physical interactions in the upper ocean: the role of vertical and small scale transport processes. *Ann. Rev. Fluid Mech.*, **27**, 225–255, 1995.

Deutsch, C.V. and A.G. Journel, *GSLIB: Geostatistical Software Library and User's Guide*, Oxford University Press, New York, NY, 340 p., 1992.

Doney, S.C., D.M. Glover and R.G. Najjar, A new coupled, one-dimensional biological-physical model for the upper ocean: Applications to the JGOFS Bermuda Atlantic Time Series (BATS) site, *Deep-Sea Res. II*, **43**, 591–624, 1996.

Doney, S.C., An atmospheric surface forcing and physical upper ocean model for the JGOFS Bermuda Atlantic Time-series Study (BATS) site, *J. Geophys. Res.*, **101**, 25,615–25,634, 1996.

Doney, S.C., Major challenges confronting marine biogeochemical modeling, *Global Biogeochem. Cycles*, **13**, 705–714, 1999.

Emery, W.J., Lee, W.G., and Magaard, L., Geographic and seasonal distributions of Brunt-Vaisala frequency and Rossby radii in the North Pacific and North Atlantic, *J. Phys. Oceanogr.*, **14**, 294–317, 1984.

Falkowski, P. G., D. Ziemann, Z. Kolber and P. K. Bienfang, Role of eddy pumping in enhancing primary production in the ocean. *Nature*, **352**, 55–57, 1991.

Feldman, G., N. Kuring, C. Ng, W. Esaias, C. McClain, J. Elrod, N. Maynard, D. Endres, R. Evans, J. Brown, S. Walsh, M. Carle and G. Podestra, 1989: Ocean color, availability of the global data set. *EOS Trans., Am. Geophys. Union*, **70**, 634–641.

Fiedler, P. C., F. P. Chavez, D. W. Behringer, and S. B. Reilly, 1992: Physical and biological effects of Los Ninos in the eastern tropical Pacific, 1986–1989. *Deep-Sea Res.*, **39**, 199–219.

Fu, L.-L. and Smith, R.D., Global ocean circulation from satellite altimetry and high-resolution computer simulation, *Bull. Amer. Meteor. Soc.*, **77**, 2625–2636, 1996.

Fuentes, M., S.C. Doney, D.M. Glover, and S.J. McCue, 2000: Spatial structure of the SeaWiFS ocean color data for the North Atlantic Ocean, *Studies in the Atmospheric Sciences (Lecture Notes in Statistics Vol. 144)*, ed. M. Berliner, D. Nychka, and T. Hoar, Springer-Verlag, New York, 153–171.

Gandin, L.S., *Objective Analysis of Meteorological Fields*, Gidrometeorologicheskoe Izdatel'stvo (GIMIZ), Leningrad (translated by Israel Program for Scientific Translations, Jerusalem, 1965), 1963.

Garcon, V.C., A. Oschlies, S.C. Doney, D. McGillicuddy, J. Waniek, The role of mesoscale variability on plankton dynamics, *Deep-Sea Res. II*, *in press.*

Gargett, A. E. 1991: Physical processes and the maintenance of nutrient-rich euphotic zones. *Limnol. Oceanogr.*, **36**, 1527–1545.

Garver, S.A. and Siegel, D.A., Inherent optical property inversion of ocean color spectra and its biogeochemical interpretation 1. Time series from the Sargasso Sea, *J. Geophys. Res.*, **102**, 18607–18625, 1997.

Glover, D.M. and S.C. Doney, 1996b, The aliasing of mesoscale spatial variability into time-series data: Satellite based estimates for the JGOFS-BATS site, *Trans. Am. Geophys. Union*, **77**(46): F402–F403.

Haury, L.R., McGowan, J.A., and Wiebe, P.H., Patterns and Processes in the Time-space Scales of Plankton Distributions, in *Spatial Patterns in Plankton Communities*, Plenum Press, New York, 277–327, 1978.

Hooker, S.B. and Esaias, W.E., An overview of the SeaWiFS project, *EOS, Trans. Amer. Geophys. Union*, **74**, 241–246, 1993.

Hooker, S.B. and C.R. McClain, The calibration and validation of SeaWiFS data, *Prog. Oceanogr.*, **45**, 427–465, 2000.

Journel, A.G. and Ch. J. Huijbregts, 1978, *Mining Geostatistics*, Academic Press, Harcourt Brace Jovanovich Publishers, New York, NY, 600 pg.

Krauss, W., Doscher, R., Lehmann, A. and Viehoff, T., On eddy scales in the eastern and northern North Atlantic Ocean as a function of latitude, *J. Geophys. Res.*, **95**, 18,049–18,056, 1990.

Kyriakidis, P.C. and Journel, A.G., Geostatistical space–time models: A review, *Math. Geology*, **31**, 651–684, 1999.

Levy, M., M. Laurent, and J.-M. Andre, Simulation of primary production and export fluxes in the northwestern Mediterranean Sea, *J. Mar. Res.*, **56**, 197–?, 1998.

Longhurst, A., S. Sathyendranath, T. Platt, and C. Caverhill, 1995: An estimate of global primary production in the ocean from satellite radiometer data. *J. Plankton Res.*, *17*, 1245–1271.

Mann, K.H. and J.R.N. Lazier, 1991: *Dynamics of Marine Ecosystems*, Blackwell Scientific Publications, Inc., Cambridge, MA, 466 pp.

Matheron, G., The theory of regionalized variables and its applications, *Fontainebleau, Les Cahiers du Centre de Morphologie Mathématique*, **5**, 1971.

McClain, C.R., Cleave, M.L., Feldman, G.C., Gregg, W.W., Hooker, S.B., and Kuring, N., Science quality SeaWiFS data for global biosphere research, Sea Technology, **39**, 10–14, 1998.

McClain, C. R., W. E. Esaias, G. C. Feldman, J. Elrod, D. Endres, J. Firestone, M. Darzi, R. Evans, and J. Brown, 1990: Physical and biological processes in the North

Atlantic during the first GARP global experiment. *J. Geophys. Res.*, **95**, 18,027–18,048.

McGillicuddy, D.J. Jr., V.K. Kosnyrev, J.P. Ryan, and J.A. Yoder, Covariation of mesoscale ocean color and sea surface temperature patterns in the Sargasso Sea, *Deep-Sea Res. II*, **submitted**, 2001.

McGillicuddy, D.J. Jr., Robinson, A.R., Siegel, D.A., Jannasch, H.W., Johnson, R., Dickey, T.D., McNeil, J., Michaels, A.F., and Knap, A.H., Influence of mesoscale eddies on new production in the Sargasso Sea, *Nature*, **394**, 263–266, 1998.

Mejia, J.M. and Rodriguez-Iturbe, I., Correlation links between normal and log normal processes, *Water Resources Res.*, **10**, 689–690, 1974.

O'Reilly, J.E., Maritorena, S., Mitchell, B.G., Siegel, D.A., Carder, K.L., Garver, S.A., Kahru, M., and McClain, C., Ocean color chlorophyll algorithms for SeaWiFS, *J. Geophys. Res.*, **103**, 24,937–24,953, 1998.

Okubo, A., *Diffusion and Ecological Problems: Mathematical Models*, Springer-Verlag, Berlin, 1980.

Press, W.H., S.A. Teukolsky, W.T. Vetterling, and B.P. Flannery, 1992: *Numerical Recipes in Fortran*, 2nd edition, Cambridge University Press, New York, USA, 963pp.

Smith, R.C., X. Zhang and J. Michaelsen, Variability of pigment biomass in the California Current system as determined by satellite imagery: 1, Spatial variability, *J. Geophys. Res.*, **93**, 10863–10882, 1988.

Smith, R.D., Maltrud, M.E., Bryan, F.O., and Hecht, M.W., Numerical simulation of the North Atlantic at $1/10^\circ$, *J. Phys. Oceanogr.*, **30**, 1532–1561, 2000.

Stammer, D., Global characteristics of ocean variability estimated from regional TOPEX/POSEIDON altimeter measurements, J. Phys. Oceanogr., **27**, 1743–1769, 1997.

Steele, J.H., *Spatial Patterns in Plankton Communities*, Plenum Press, New York, 1978.

Sullivan, C.W., K.R. Arrigo, C.R. McClain, J.C. Comiso, and J. Firestone, 1993: Distributions of phytoplankton blooms in the Southern Ocean. *Science*, 1832–1837.

U.S. JGOFS Planning Report Number 14, 1992: Report of the U.S. JGOFS Workshop on Modeling and Data Assimilation, Mark R. Abbott, Chariman, U.S. JGOFS Planning Office, Woods Hole, MA, 28 pp.

Uz, M., J.A. Yoder, and V. Osychny, Pumping of nutrients to ocean surface waters by the action of propagating planetary waves, *Nature*, **409**, 597–600, 2001.

Washburn, L., Emery, B.M., Jones, B.H., and Ondercin, D.G., Eddy stirring and phytoplankton patchiness in the subartic North Atlantic in late summer, *Deep-Sea Research I*, **45**, 1411–1439, 1998.

Woods, J.D., Mesoscale upwelling and primary production, In: *Toward a theory of physical–biological interactions in the world ocean*, B.J. Rothschild, ed., Kluwer Academic Publishers, London, 650pp., 1988.

Wroblewski, J., A model of the spring bloom in the North Atlantic and its impact on ocean optics, Limnol. Oceanogr., **34**, 1563–1571, 1989.

Yaglom, A.M., Some classes of random fields in n-dimensional space, related to stationary random processes, *Theory of Probability and Its Applications*, **2**, 273–320, 1957.

Yoder, J.A., An overview of temporal and spatial patterns in satellite-derived chlorophyll-a imagery and their relation to ocean processes, In: *Satellites, Oceanography and Society*, ed. D. Halpern, 225–238, 2000.

Yoder, J.A., S.G. Ackleson, and W.M. Balch, A line in the sea, *Nature*, **371**, 689–?, 1984.

Yoder, J.A., McClain, C.R., Blanton, J.O., and Oey, L.-Y., Spatial scales in CZCS-chlorophyll imagery of the southeastern U.S. continental shelf, *Limnol. Oceanogr.*, **32**, 929–941, 1987.

Yoder, J.A., C.R. McClain, G.C. Feldman, and W.E. Esaias, Annual cycles of phytoplankton chlorophyll concentrations in the global ocean: A satellite view. *Global Biogeochem. Cycles*, **7**, 181–193, 1993.

Yoder, J.A., J.E. O'Reilly, A.H. Barnard, T.S. Moore, and C.M. Ruhsam, Variability in Coastal Zone Color Scanner (CZCS) chlorophyll imagery in ocean margin waters off the U.S. East Coast, *Prog. Oceanogr.*, **submitted**, 2000.

S. C. Doney, Climate and Global Dynamics, National Center for Atmospheric Research, Boulder, CO 80307. (e-mail: doney@ncar.ucar.edu)

D. M. Glover and S. J. McCue, Marine Chemistry and Geochemistry, Woods Hole Oceanographic Institution, Woods Hole, MA 02543. (e-mail: david@plaid.whoi.edu)

M. Fuentes, Department of Statistics, North Carolina State University, Raleigh, NC 27965. (e-mail: fuentes@stat.ncsu.edu)

Received —; revised —; accepted —.

This preprint was prepared with AGU's LaTeX macros v5.01. File struct formatted February 14, 2001.

List of Figures

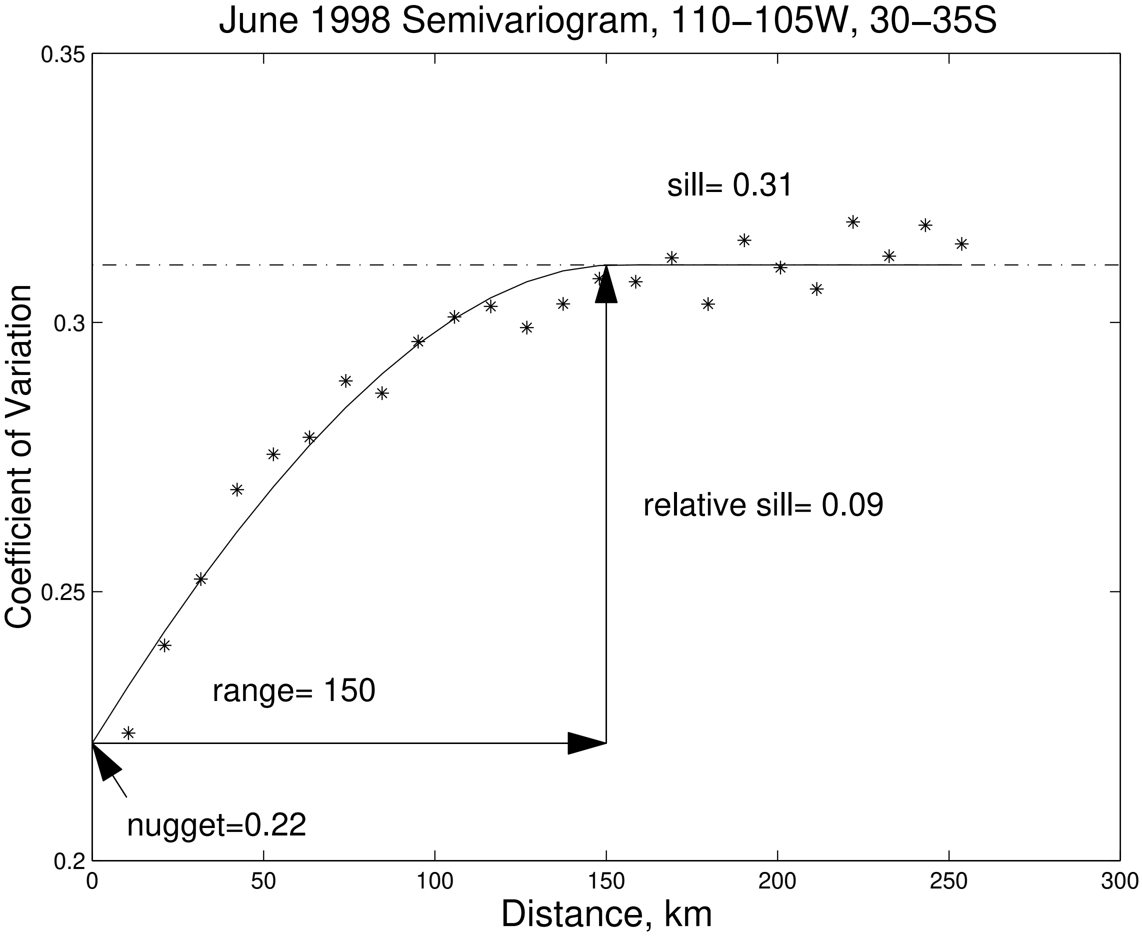

Figure 1. ../figures/fig_box_spherical.eps

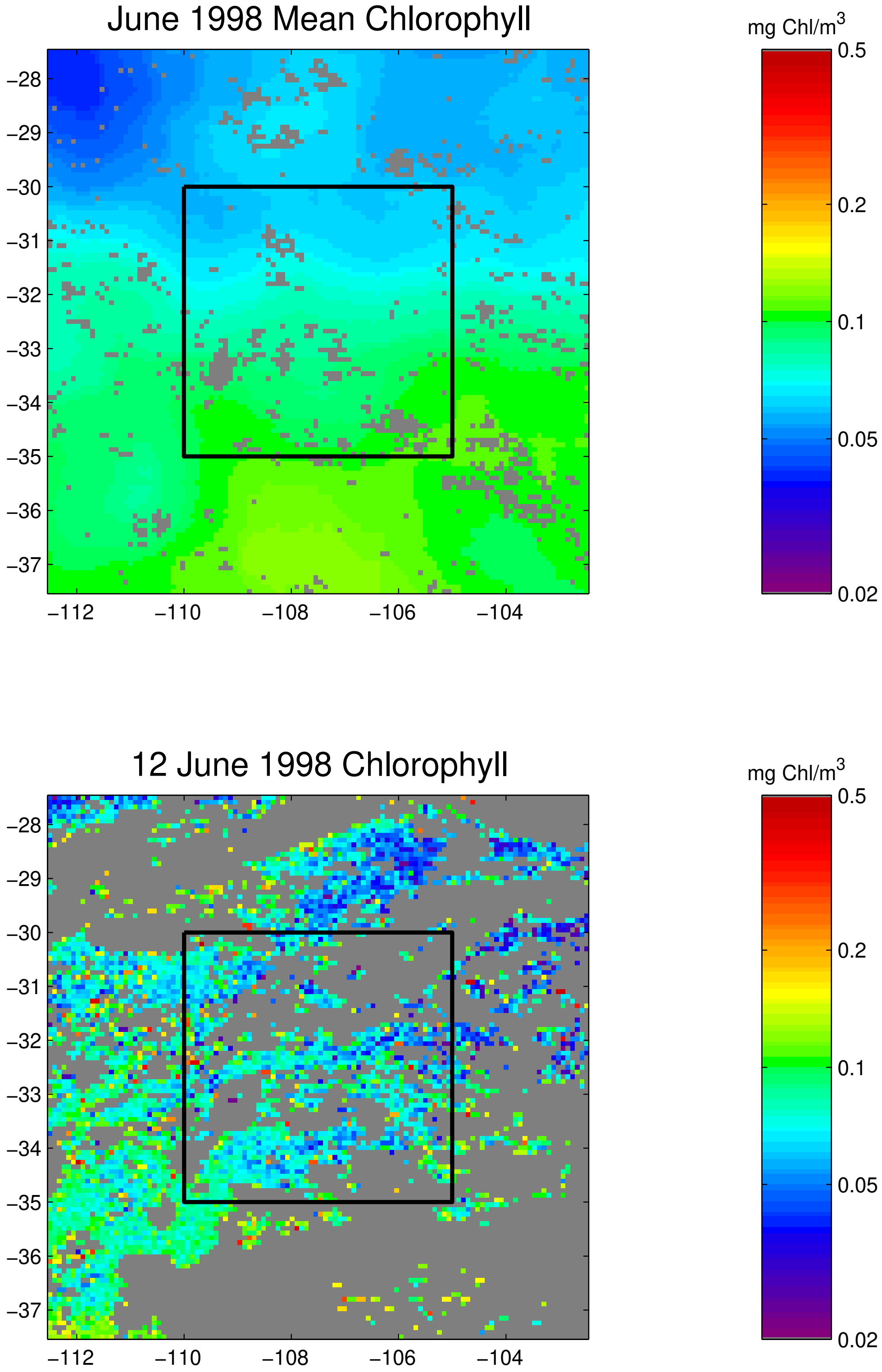

Figure 2. ../figures/fig_box_chl_map.eps

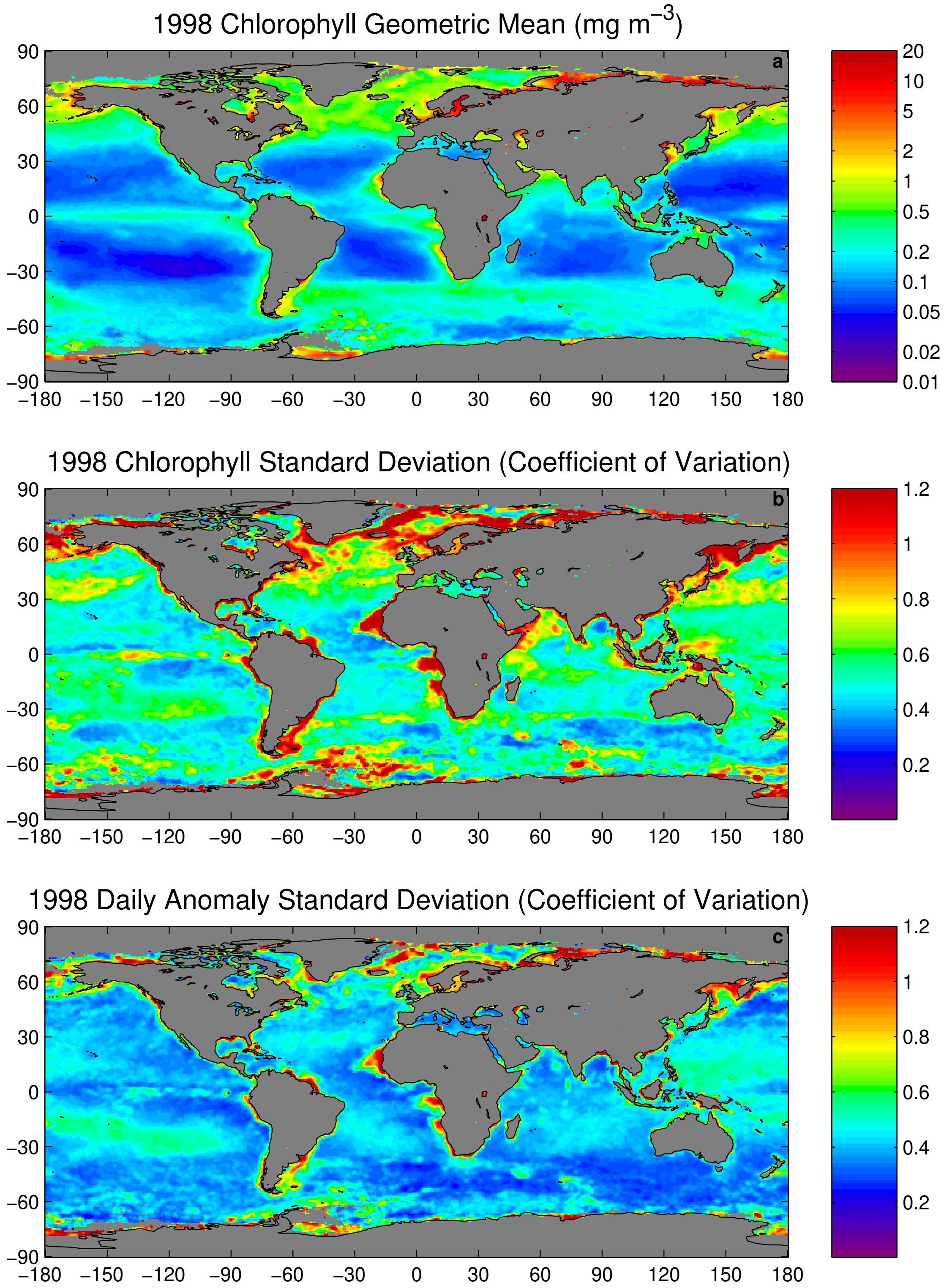

Figure 3. ../figures/fig_globe_mean.eps

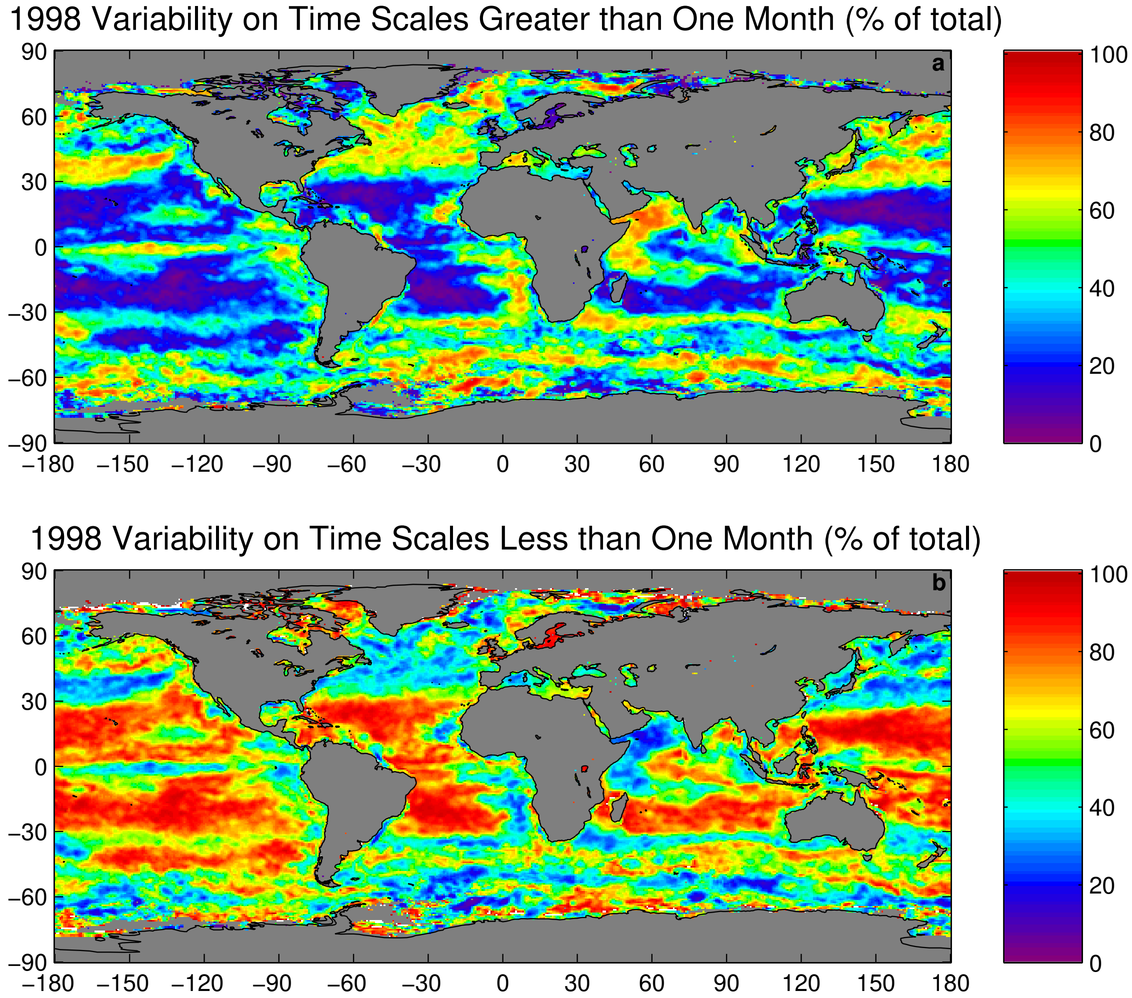

Figure 4. ../figures/fig_globe_percent.eps

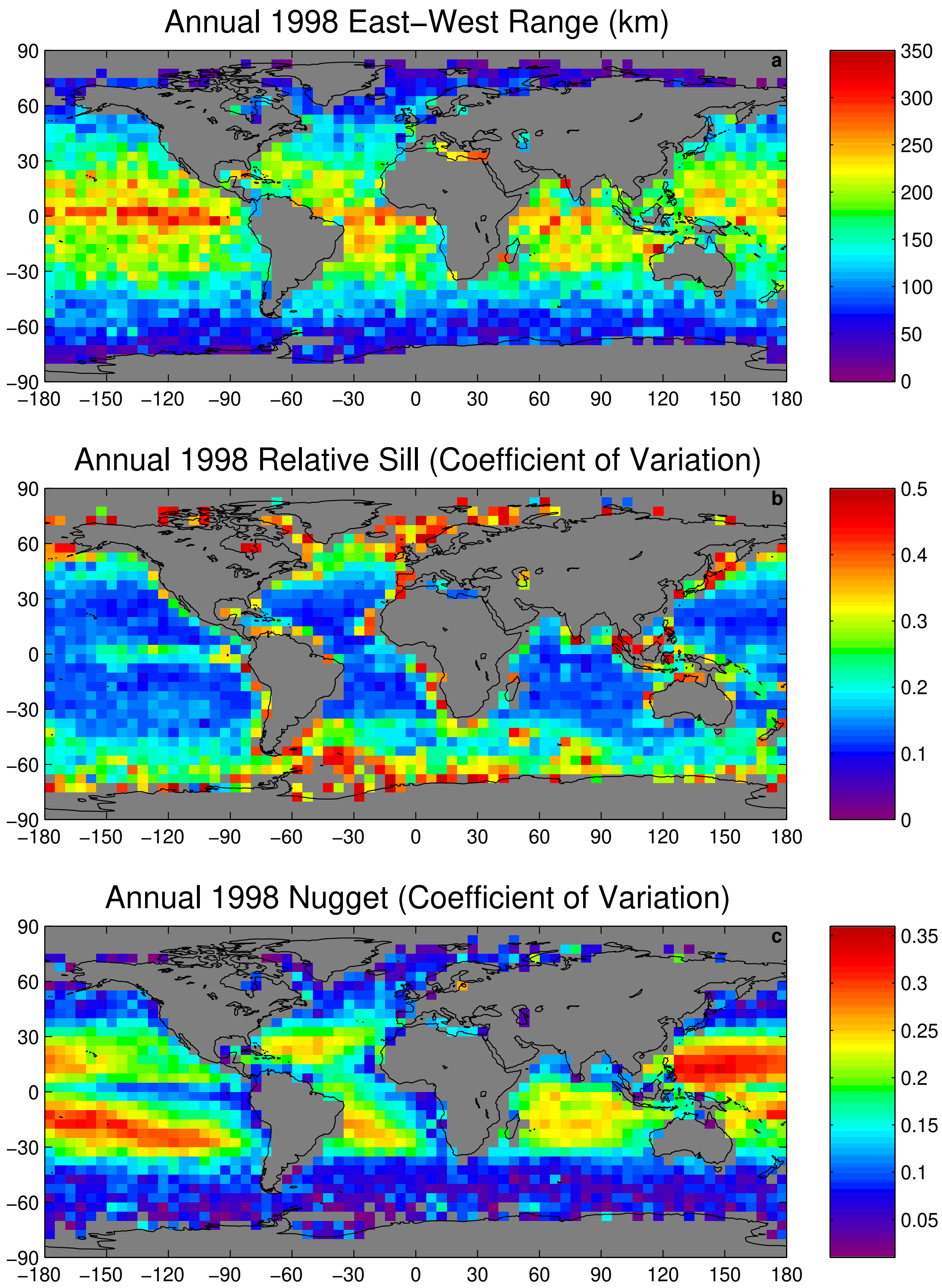

Figure 5. ../figures/semivar_global_rel.eps

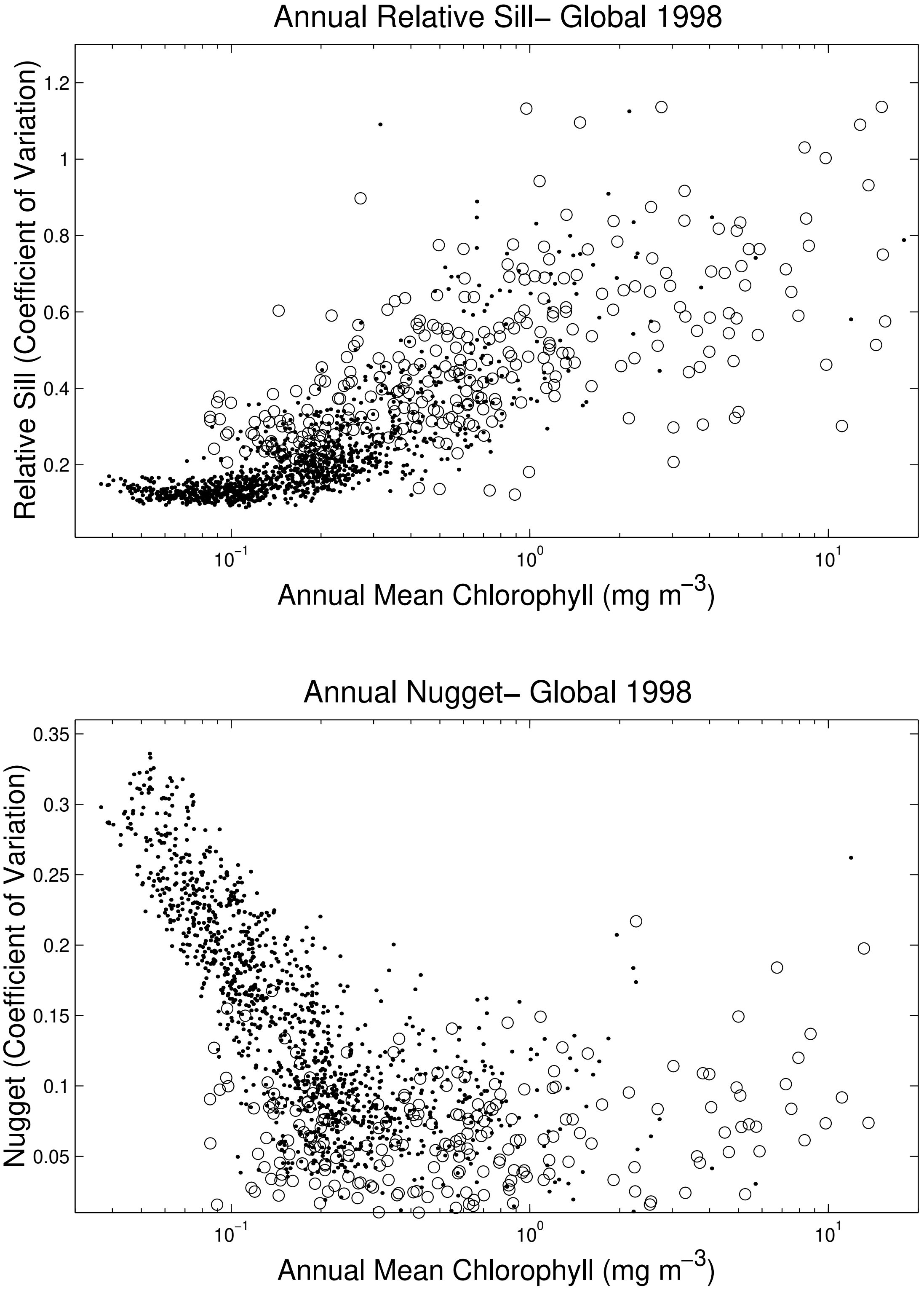

Figure 6. ../figures/semivar_scatter.eps

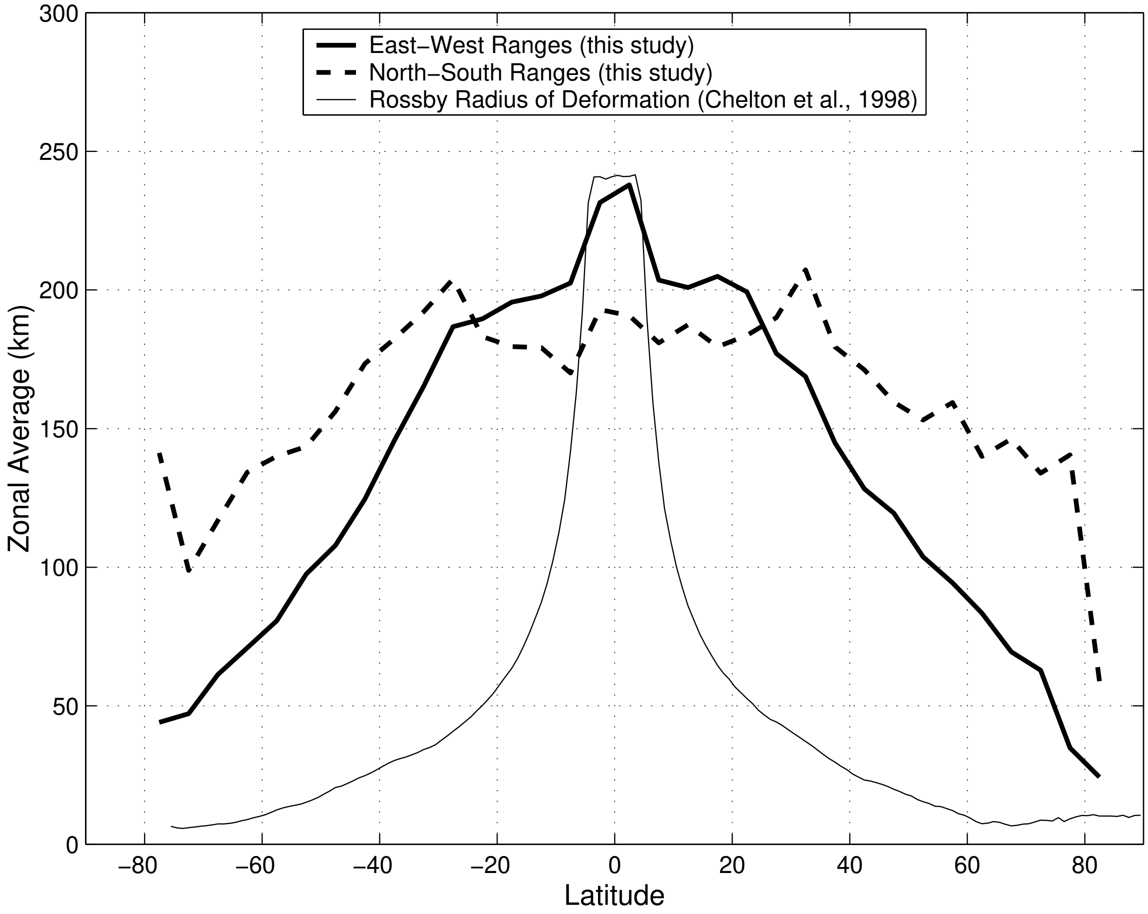

Figure 7. ../figures/zonal_scales.eps